A machine-learning approach to predicting and understanding the properties of amorphous metallic alloys

Jie Xiong [b], San-Qiang Shi [b,*], Tong-Yi Zhang [a,*]

[a] Material Genome Institute, Shanghai University, Shanghai, China
[b] Department of Mechanical Engineering, The Hong Kong Polytechnic University, Hong Kong, China

HIGHLIGHTS

- The machine learning based models for predicting properties of metallic glasses are developed.
- Key features are selected, and expressions based on those features are generated.
- The machine learning based models and expressions show good predictive and generalization ability.

GRAPHICAL ABSTRACT
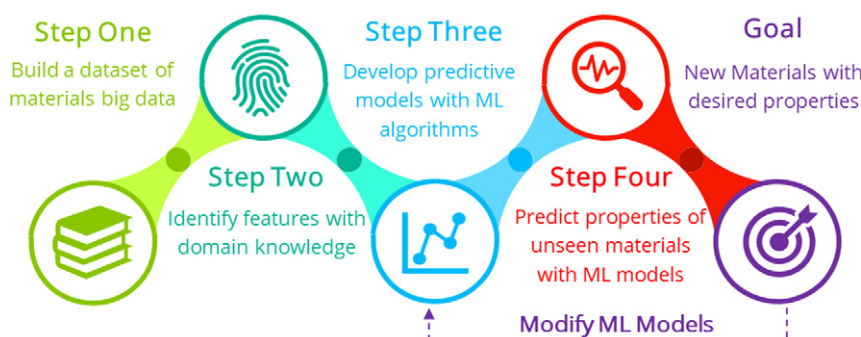
ARTICLE INFO

ABSTRACT

There is a pressing need to shorten the development period for new materials possessing desired properties. For example, bulk metallic glasses (BMGs) are a unique class of alloy materials utilized in a wide variety of applications due to their attractive physical properties. However, the lack of predictive tools for uncovering the relationships between BMGs' alloy composition and desired properties limits the further application of these materials. In this study, a machine-learning (ML) approach was developed, based on a dataset of 6471 alloys, to enable the construction of a predictive ML model to describe the glass-forming ability and elastic moduli of BMGs. The model's predictions of unseen data were found to be in good agreement with most experimental values. Consequently, we determined that an alloy with a large critical-casting diameter would likely have a high mixing entropy, a high thermal conductivity, and a mixing enthalpy of approximately -28 kJ/mol, and that a BMG with a small average atomic volume would likely have a high elastic modulus. The efficacy of ML was demonstrated in furnishing a mechanistic understanding and enabling the prediction of metallic-glass properties.

© 2019 Brunel Centre for Advanced Solidification Tecnhnology, Brunel University London. Published by Elsevier Ltd. This is an open access article under the CC BY-NC-ND license (http://creativecommons.org/licenses/by-nc-nd/4.0/).

1. Introduction

The amorphous structure of metallic glasses results in distinct mechanical and physical properties that are not exhibited by conventional crystalline alloys. For example, the disordered structure leads to high yield strength and wear resistance [1,2], high magnetic permeability

* Corresponding authors.
  E-mail addresses: san.qiang.shi@polyu.edu.hk (S.-Q. Shi), zhangty@shu.edu.cn (T.-Y. Zhang).

[3], and high corrosion resistance [4] in some metallic glasses, meaning that bulk metallic glasses (BMGs) are promising materials for engineering applications. Paradoxically, however, the absence of structural order in metallic glasses is not conducive to their bulk manufacture, which hinders their use and application. Fewer than 1000 BMGs have been developed in the last 50 years, and many of these comprised multiple components; indeed, BMGs usually contain three or more components [5]. In addition, the nonequilibrium nature of the amorphous phase indicates that various processing parameters, such as cooling rates and enhanced surface diffusion, affect the formation ability of amorphous metallic glass [6]. This generates an enormous combinatorial space of composition-processing parameters for BMGs, rendering a trial-and-error based design method extremely challenging.

The conventional development of metallic glasses mainly relies on experience; for instance, metallic glasses are known to form in systems near deep eutectics [7]. In recent decades, various empirical models based on factors such as thermodynamics [8–10], valence electron distribution [11], atomic size mismatches [12], and transformation temperatures [13] have provided fundamental insights into metallic glass-forming conditions. However, these models are usually limited to certain metallic glass compositions, and there is no universal model capable of predicting the glass-forming ability of unknown alloys.

Recently, machine-learning (ML) approaches have been utilized to predict the properties of metallic materials. For example, Xue et al. developed ML models to search for shape memory alloys with targeted transformation temperatures [14,15]. Cheng et al. formulated a materials design strategy combining ML models with experiments to find high entropy alloys with large hardness [16]. Feng et al. utilized a deep neural network to predict the defects in stainless steel [17]. Sun et al. developed ML models to predict the glass-forming ability of binary metallic alloys [18]. Ward et al. constructed a ML framework for accelerating the design of engineered metallic glasses and validated it via commercially viable fabrication methods [19]. Ren et al. introduced ML-based iteration and high-throughput experiments to rapidly discover new glass-forming systems [20]. Several studies have used ML approaches to identify the correlations between glass-forming ability and the experimentally measured properties of an alloy [21,22]. These studies thus confirmed that ML methods were reliable and efficient in discovering new metallic glasses and predicting their properties.

In this work, we developed and validated a general ML framework for the prediction of the properties and design of metallic glasses, based on their compositions. A dataset of metallic glasses was created by collecting data from several related studies [23–34] and the Landolt-Bornstein handbook on amorphous ternary alloys [35]. These data covered variables such as BMG glass-forming ability, critical casting diameter, and elastic properties. ML tools such as random forest (RF) and symbolic regression were used to create models for predicting the desired properties of metallic glass compositions. Key descriptors or features were screened by a three-step selection method during model constructions, and symbolic regression was used to develop mathematical expressions based on these features. This ML framework was shown to accelerate the development of new metallic glass-forming systems and provide a greater understanding of the physics underpinning the properties of metallic glasses.

2. Method

2.1. Data collection

The data on BMGs were collected from several publicly available resources and partitioned into four training sets: glass-forming ability (GFA); critical casting diameter (D_{max}); characteristic transformation temperatures (CTTs); and elastic moduli (EM). The training sets represented a wide range of elements, including metals and metalloids, with the GFA and D_{max} datasets containing 54 elements, the CTT datasets containing 42 elements, and the EM datasets containing 48 elements (Fig. 1).

GFA describes whether an alloy can form an amorphous bulk (i.e., a BMG) via rapid cooling (e.g., by copper-mold casting, injection molding, or suction casting), an amorphous ribbon (i.e. a ribbon metallic glass, or RMG), or a crystalline alloy (CRA). If there have been conflicting reports about the GFA of individual alloys, the highest GFA was selected for our dataset. For example, $Al_{25}Gd_{55}Ni_{20}$ was reported in the Landolt-Bornstein handbook [35] to form an RMG, but Fang et al. found that this alloy can form a bulk sample with a diameter of 3 mm [32], so it was denoted a BMG in our dataset. This GFA dataset consisted of 6471 unique alloy compositions in total, comprising 1211 BMGs, 1552 CRAs, and 3708 RMGs.

In terms of physical metallurgy, the critical cooling rate of an alloy is the most reliable and quantifiable measurement of its GFA [34]. This is the slowest cooling rate above which no crystallization occurs during the solidification of an alloy, and is determined using data from multiple solidifications at different cooling rates. D_{max} is a slightly less rigorous parameter and much easier to experimentally obtain than the critical cooling rate, as it is the largest diameter or the largest section-thickness of an alloy when it is cast into a fully amorphous rod or plate. In general, the slower the cooling rate, the larger the D_{max}, and the higher the GFA.

The D_{max} dataset contained values for 5934 entries. For BMG alloys, only the critical copper-mold casting diameter values reported in the literature were included, i.e., the D_{max} of samples from injection molding and suction casting were not considered. For RMG alloys, a single and small value of 0.1 mm for D_{max} was assumed as appropriate for this dataset, as this was half the D_{max} of the smallest reported BMG, $Ti_{50}Cu_{42.5}Ni_{7.5}$ [34]. The D_{max} of CRAs was set at 0. As with the GFA dataset, if there were multiple values of D_{max}, the highest was used.

Various criteria have been proposed to compare the GFA of alloys, with most based on CTTs [36]. Varying combinations of transformation temperatures have been found to determine the relationship of D_{max} to GFA criteria, such as the supercooled liquid range $\Delta T = T_x - T_g$ [36] and the reduced glass transition temperature $T_{rg} = T_g/T_l$ [37]. Here, T_g is the glass transition temperature, T_x is the onset of crystallization temperature, and T_l is the liquidus temperature. The CTT dataset was assembled from 674 measurements of differential thermal analysis or differential scanning calorimetry at a constant heating rate, with most of the entries obtained at rate of 20 K/min. When multiple values of a CTT were reported, their averaged value was used here.

The EM data included the shear moduli G and bulk moduli B of BMGs. The ratio of G to B correlated with the fracture toughness, intrinsic plasticity, and GFA of metallic glasses [34]. The Young's moduli can be calculated with G and B based on the isotropic mechanical property of BMGs. In addition, strong linear relationships between fracture tensile strength and Young's moduli, hardness and Young's moduli, yield shear stress and shear moduli were found in the previous works [34,38,39]. The EM dataset contained 278 unique BMGs, and their moduli were measured with resonant ultrasonic spectroscopy (RUC). The dataset shows all reported values of a property for each given alloy, indicating that there are multiple values for some properties of a given alloy. However, the difference between the multiple values is small. To simplify the following ML process, the average of multiple values was used for such property of a particular BMG. For example, the values of shear modulus of $Mg_{65}Cu_{25}Tb_{10}$ were 19.4 GPa and 19.6 GPa reported by Wang et al. [34] and Chen et al. [39], respectively. Thus, the mean of 19.5 GPa was used in the following analysis for the shear modulus of $Mg_{65}Cu_{25}Tb_{10}$.

2.2. Feature candidates

Candidate features (X) are the input for an ML model (f) to predict the desired properties (Y), i.e., $Y = f(X)$. Thus, for a given target property Y, an adequate set of X had to be identified to ensure that a well-

Fig. 1. The elements included in the four constructed datasets, which described a BMG alloy in terms of its GFA (red fill), D_{max} (green fill), CTT (yellow fill), and EM (blue fill).

performing ML model was generated. As the physics underlying the glass transformation of an alloy are not well understood, as many potential descriptions as possible should be included to predict the GFA and D_{max}. The feature candidates of an alloy were thus compiled with the basic elemental parameters, thermodynamic parameters, valence electron distribution, and atomic volume of the alloy elements.

The elemental parameters were based on the elemental properties from experiments or density functional theory (DFT) simulations, and comprised, inter alia, atomic fundamental properties (e.g., atomic number, period, group in the periodic table), chemical properties (e.g., Pauling electronegativity, Mulliken electronegativity), and physical properties (density, melting temperature, specific heat capacity). The alloy feature candidates were calculated from the corresponding elemental properties (shown in Table 1) based on the linear mixture rule (x_1) [40] and the reciprocal mixture rule (x_2) [41], and their deviation (xD) [42] and discrepancy (xd) were also calculated [42], with Eqs. (1)–(4).

$$x_1 = \sum_{i=1}^{N} a_i x_i \tag{1}$$

$$x_2 = \left(\sum_{i=1}^{N} \frac{a_i}{x_i} \right)^{-1} \tag{2}$$

$$xD = \sqrt{\sum_{i=1}^{N} a_i (x_i - x_1)^2} \tag{3}$$

$$xd = \sqrt{\sum_{i=1}^{N} a_i (1 - x_i/x_1)^2}, \tag{4}$$

Table 1
The used 20 basic elemental properties and their values can be seen in Table S1.

Elemental Property (Abbreviation)		
Atomic number (AN)	Density (D)	Mulliken electronegativity (X_M)
Atomic weight (AW)	Melting point (T_m)	Pauling electronegativity (X_P)
Group (Gp)	Boiling point (T_b)	First ionization potential (I_1)
Period (P)	Heat capacity (C_p)	Second ionization potential (I_2)
Covalent radius (R_c)	Thermal conductivity (K)	Electron affinity (E_{ea})
Metallic radius (R_m)	Heat of fusion (H_f)	Work function (W)
Valence electrons (VEC)	Lattice volume (LP)	

where a_i and x_i are the atomic fraction and elemental properties of the i-th constituent, respectively.

Thermodynamic parameters reflect the driving force for glass transformation, and these parameters (which are defined in the equations below) include the mixing enthalpy (H_{mix}) based on Miedema's empirical method [43] (Eq. (5)), the normalized mixing entropy (S_{mix}/R), based on fundamental thermodynamics [44] (Eq. (6)), the normalized mismatch entropy (S_{mis}/k_B), estimated via a relationship given by Takeuchi et al. [12] (Eq. (7)), as well as two parameters denoted PHS_{mis} (Eq. (8)) and $PHSS$ (Eq. (10)) proposed by Rao et al. [45], and a similar self-defined parameter PHS_{mix} (Eq. (9)):

$$H_{mix} = 4 \sum_{j=i}^{N} \sum_{i=1}^{N} \Delta H_{ij} a_i a_j \tag{5}$$

$$S_{mix}/R = - \sum_{i=1}^{N} a_i \ln a_i \tag{6}$$

$$S_{mis}/k_B \cong (R_m d)^2 / 21.92 \tag{7}$$

$$PHS_{mis} = H_{mix} \cdot S_{mis}/k_B \tag{8}$$

$$PHS_{mix} = H_{mix} \cdot S_{mix}/R \tag{9}$$

$$PHSS = H_{mix} \cdot S_{mis}/k_B \cdot S_{mix}/R, \tag{10}$$

where ΔH_{ij} is the molar mixing enthalpy for binary liquid alloys [12], R is the gas constant, k_B is the Boltzmann constant, $R_m d$ is the discrepancy of R_m calculated with Eq. (4).

The valence electron distributions comprised the number ($sVEC$, $pVEC$, $dVEC$) and the fraction (f_s, f_p, f_d) of electrons in the s, p, d valence orbitals of an element, based on the linear mixture rule [46], as given by Eq. (11). The equation for the average atomic volume (V_{mm} and V_{mc}) was constructed by Wang et al. [47] to predict the bulk modulus, which may affect the GFA, and is given by Eq. (12):

$$f_{(s,p,d)} = (s, p, d) VEC / VEC_1 \tag{11}$$

$$V_{m(m,c)} = \sum_{i=1}^{N} a_i \cdot \frac{4}{3} \pi R_{(m,c)}^3 \tag{12}$$

where VEC_1 is the average number of valence electrons, as calculated by Eq. (1).

In summary, 94 feature candidates, termed as zero-generation features, were generated for further study.

2.3. Feature scaling

As the range of magnitudes of the generated feature candidate alloys varied broadly, the use of Euclidian distances in computations such as decision trees, neural networks, and K-nearest neighbors (KNN), typical of some ML models, may not be appropriate. Therefore, the feature-scaling method was adopted to normalize the scale of features, thus serving as a preprocessing step prior to feature selection and model construction [48]. The min-max normalization (or min-max rescaling) method was applied to rescale features in this work, and the feature candidate alloys were scaled to a predefined domain [a, b], according to Eq. (13):

$$x' = a + \frac{(b-a)(x- \min x)}{\max x - \min x} \tag{13}$$

where $a = 0.2$, $b = 0.8$, x is the original feature, x' is the normalized feature, and min x and max x are the minimum and maximum value of the original feature. Tang et al. [49] found that the general domain [0, 1] might affect the performance of some ML algorithms, e.g. neural networks, and they recommended the use of smaller domains, such as [0.2, 0.8].

2.4. Feature selection

Feature selection is a key process that has a critical effect on the performance of the ML model. It involves selecting a subset of relevant features for model construction, and enables some irrelevant features to be discarded with minimal loss of information. Thus, a three-step feature-selection method (TFS) was adopted to screen the normalized feature candidates in the GFA and D_{max} dataset (as shown in Fig. 2).

Initially, a feature that is highly correlated with other features can be considered to contain similar information. Thus, a correlation-based feature selection (CFS) method was used to remove these redundant features. The Pearson correlation coefficient (PCC) is a measurement of the linear correlation between two features X_1 and X_2, and is given by Eq. (14):

$$PCC(X_1, X_2) = \frac{E[(X_1-E[X_1])(X_2-E[X_2])]}{\sigma_{X_1}\sigma_{X_2}}, \tag{14}$$

where σ_{X_1} and σ_{X_2} denote the standard deviation of features X_1 and X_2, and E is the expectation. PCC has a value between -1 and 1, where -1 represents a wholly negative linear correlation, 1 represents a wholly positive linear correlation, 0 represents no linear correlation, and a value > 0.75 or <-0.75 indicates a strong correlation. The highly cross-correlated features are thus revealed and able to be removed, and the remaining n features are denoted the first-generation features. The selection of the first-generation features is also based on domain knowledge. For example, metallic glass structures are generally built based on a hard spheres model, wherein the atoms are assumed to be densely and randomly packed. Thus, R_{c1} is removed when it is highly correlated with R_{m1}.

After this, a widely used filter method known as variance threshold (VT) was adopted to further screen the first-generation features. The VT method assumes that a low-variance feature generally has very little predictive power, and thus m features whose variance (Var) is below a certain threshold (as determined by Eq. (15) below) are removed:

$$Var(X) = E\left[(X-E[X])^2\right]. \tag{15}$$

The ReliefF feature selection algorithm [50] searches for k nearest neighbor samples from the same class $H(x)$, and for k nearest neighbors from each different class $M(x)$. During this process, the weights of features are adjusted by comparing in-class distances and inter-class distances after N iterations. This procedure is given by

$$W_f^N = W_f^{N-1} + \left(\sum_{C \neq Class(x)} \frac{P(x)}{1-P(class(x))} \frac{\sum_{i=1}^{k}|x-M_i(x)|}{Nk \cdot range(x)} \right) - \frac{\sum_{j=1}^{k}|x-H_j(x)|}{Nk \cdot range(x)}, \tag{16}$$

where $P(x)$ is the probability of x, and $range(x)$ is the difference between the maximum value and minimum value of each feature, which is 0.6 for the normalized features in this study. Next, a subset containing (n-m) features is selected using of the ReliefF algorithm to accurately
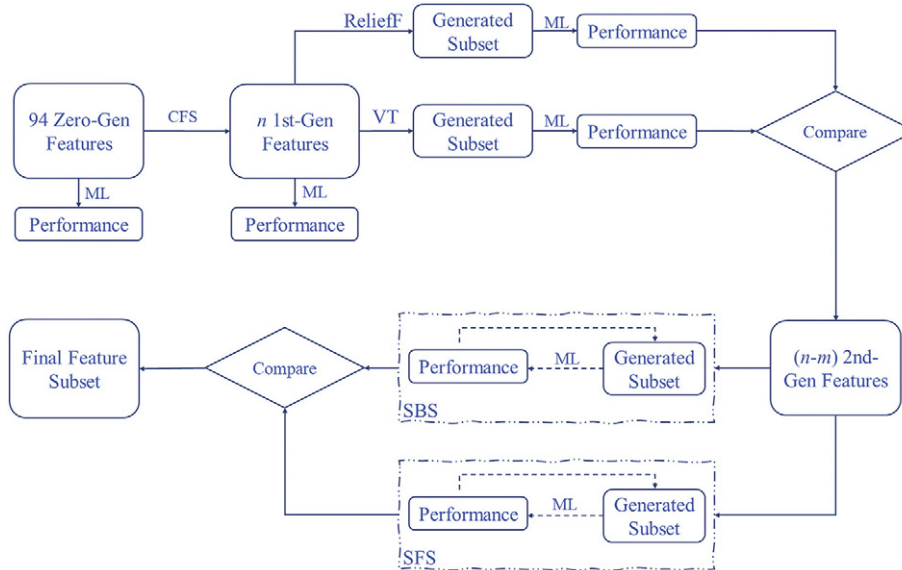

Fig. 2. The three-step feature selection method, involving the selection of first-generation features by correlation-based feature selection from the feature candidates, followed by the selection of second-generation features by comparison of the performance of the variance threshold and the ReliefF algorithm, and finally the determination of the final feature subset by comparing the results of sequential forward selection (SFS) and sequential backward selection (SBS).

compare the performance of these features, and the results are denoted the second-generation features.

Finally, wrapper methods were used to determine the final feature subsets. Wrapper methods are based on greedy search algorithms, including sequential forward selection (SFS) and sequential backward selection (SBS). These evaluate possible feature subsets and select the subset that produces the best performance for a specific ML algorithm (which was an RF in this work). Thus, for a given dimensional feature set X^*, SFS starts from the null set, and sequentially adds the best feature x^+ that maximizes the prediction accuracy (J) when combined with the already selected feature subset X^k, until the accuracy is satisfied [51]. This is expressed by

$$X^{k+1} = X^k + x^+; x^+ = \arg \max J\left(X^k + x\right), x \in X^* - X^k. \tag{17}$$

In contrast, SBS starts from the full set X^* and sequentially removes the worst feature x^- that least reduces the prediction accuracy from X^k, until the accuracy is satisfied [51], as given by

$$X^{k-1} = X^k - x^-; x^- = \arg \max J\left(X^k - x\right), x \in X^k. \tag{18}$$

2.5. Machine learning models

Around 20 ML algorithms available in the WEKA library, including linear ML algorithms (linear regression, logistic regression, elastic net, ridge regression), nonlinear ML algorithms (naive bayes, bayes net, decision tree, k-nearest neighbors, locally weighted learning, support vector machines, Gaussian regression, neural network), ensemble ML algorithms (random forest, bagging, stacking), were used evaluated in terms of second-generation features via the cross-validation test [52]. The random forest (RF) algorithm super-performed over the other ML algorithms and thus was used for further in the study. Since mathematical expressions for regression problems were not available in the RF model, symbolic regression based on genetic programming was used to distil mathematical formulas from the desired properties and chosen features [53]. The initial expressions were generated by randomly combining mathematical operators, functions, constants, and non-normalized chosen features. Next, new formulas were continuously iterated by genetic programming and finally evolve to the optimal formula.

The performance of the classification models was measured by their classification accuracy, which describes the proportion of the samples that were correctly classified. The performance of the regression models was measured by the correlation coefficient r

$$r = \sqrt{\frac{\sum_{i=1}^{n}\left(\widehat{y}_i - \overline{y}\right)^2}{\sum_{i=1}^{n}\left(y_i - \overline{y}\right)^2}} \tag{19}$$

and the root mean square error ($RMSE$)

$$RMSE = \sqrt{\sum_{i=1}^{n}\frac{1}{n}\left(\widehat{y}_i - y_i\right)^2} \tag{20}$$

where $\widehat{y}_i$ is the prediction and $\overline{y}$ is the average of y_i, and the r value lies between 0 and 1, with 1 indicating a perfect fit.

2.6. Cross-validation test

The k-fold (with $k = 100$) cross-validation (CV) test was conducted here to evaluate the performance of different ML models. The initial dataset was randomly and equally split into k sub-datasets, a training set with (k-1) sub-datasets, and a testing set with the remaining sub-datasets. The ML model was built on the training set, and the performance was measured with the testing set. This process was repeated k times, and the cross-validation accuracy was obtained by the average value of the k results; this could be regarded as an estimation of the testing accuracy.

3. Results and discussion

Here we describe the building of a classification model to determine the GFA of alloys, a regression model based on alloy composition, another regression model based on CTT to predict D_{max}, and two regression models to predict the EM of an alloy. In addition, mathematical expressions were developed by symbolic regression and the linear least-squares method for regression problems.

3.1. GFA model

The Pearson correlation coefficient (PCC) between two features X_1 and X_2 were calculated, where X_i ($i = 1, 2, 3, \ldots 94$) denotes the 94 zero-generation features, and the target variable of the GFA data was not included. Based on the PCC values between -0.75 and 0.75, 35 first-generation features were selected from the 94 zero-generation features and thus from the GFA dataset. Fig. 3c shows that the CV classification accuracy of the ML model built on the CFS subset (CFS-GFA) can reach 89.52%, which is greater than that of the ML models constructed on the feature candidates and other subsets.

However, the dimensionality of feature space must be further reduced to achieve a balance between performance and complexity, with a tolerance of 2% for CV classification accuracy. Thus, as shown in Fig. 3a and b, 14 features with a variance > 0.01 were selected by VT, and another subset containing 14 features was given by use of the ReliefF algorithm. The VT subset leads to a cross-validation classification accuracy (88.89%), more or less the same as that of 88.21% based on the ReliefF subset. Feature selection was further conducted with the two subsets by using the SBS and SFS methods. The results show that the SBS and SFS give the same subset. This feature selection yields the VT-SS-6 with the six features of VEC_1, $sVEC$, $H_f d$, T_{b2}, Gp_1, and Wd from the VT subset and the ReF-SS-6 with the six features of KD, Kd, $VECd$, Wd, S_{mix}/R, and $T_b d$ from the ReliefF subset, clearly indicating that VT-SS-6 and ReF-SS-6 have completely different features. Fig. 3c shows that the ML model with the six VT-SS-6 features (VTS6-GFA) had a CV classification accuracy of 88.13% and the ML model with the ReF-SS-6 features had a CV classification accuracy of 87.15%. The difference between the two CV classification accuracies is about 1%, although the two six-features subsets are completely different. This result might indicate that there are some correlations between the two subsets. Nevertheless, to simplify the following ML analysis, we took the VT-SS-6 subset as the final feature subset.

A good ML model should be able to provide accurate prediction with as less as possible number of features. The CFS-GFA model had the best classification accuracy of 89.52% with 36 features. The VTS6-GFA model uses only six features and has a classification accuracy of 88.13%, which indicates that the six-features play the major role in the classification, although the classification accuracy is reduced by 1.39%.

Fig. 4a shows the confusion matrix of the VTS6-GFA model, which has an accuracy of 88.13%. In this context, precision is the ratio of relevant samples to retrieved samples. For example, 1151 alloys were classified as BMG alloys by the ML model, and 1073 were labeled as BMGs in our dataset, meaning that the precision of BMG classification was 93.2%. In addition, recall or true positive rate is the fraction of retrieved relevant samples among the total relevant samples: for instance, 3463 out of 3708 RMG-labeled alloys were classified as RMG alloys by the ML model, and thus the recall of RMG was 93.4%. Thus, if one wants to use this ML model to distinguish GFAs (BMG or RMG) from non-GFAs (CRA), the precision of GFA predictions is 92.5%, and the recall can reach as high as 96.4%.
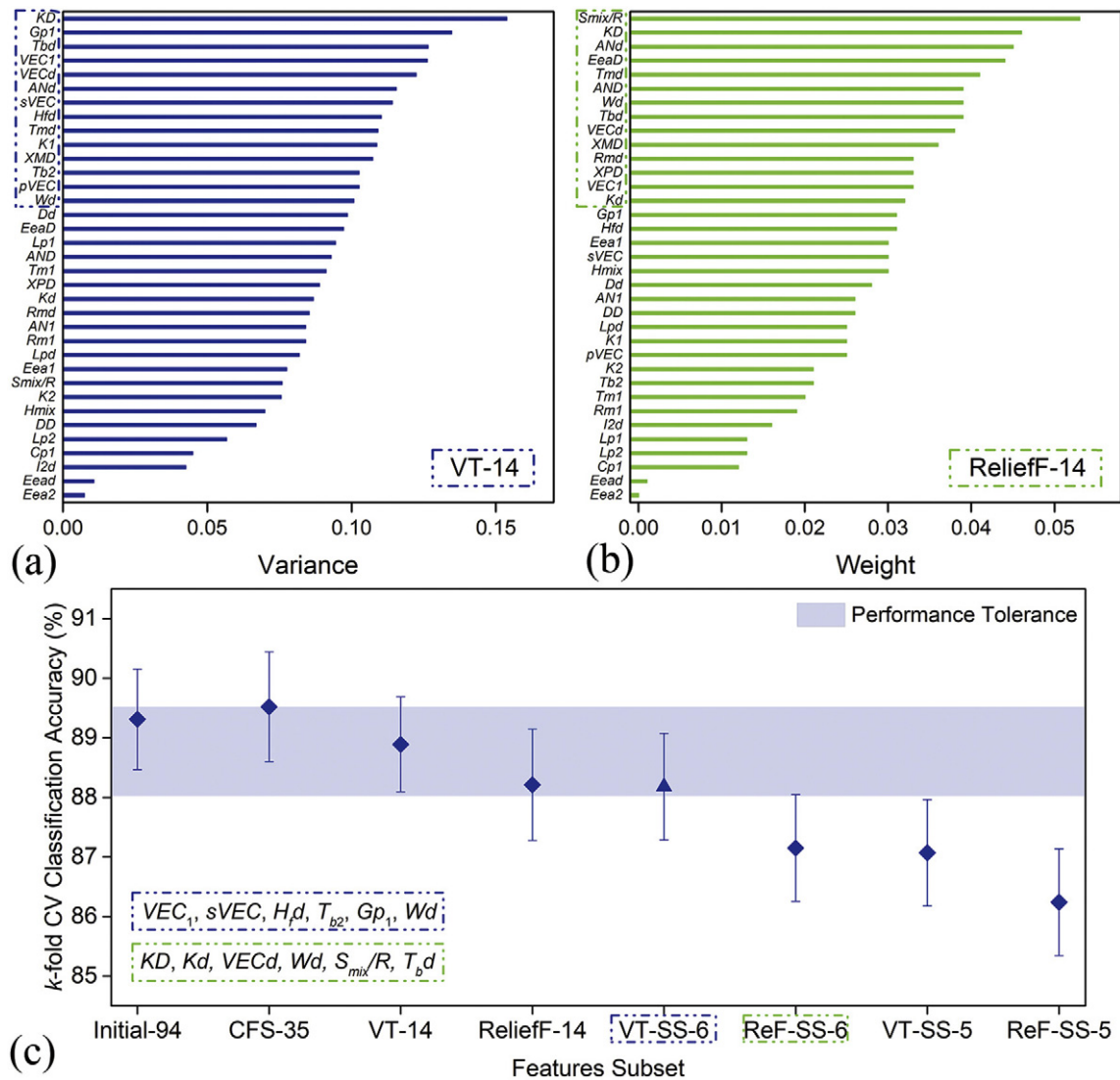
Fig. 3. (a) The variance and (b) the weight of the first-generation features. (c) The *k*-fold CV classification accuracy of a random forest model of various feature subsets.

Another widely used measurement, the receiver operating characteristic (ROC) curve, is shown in Fig. 4b. The ROC curve is created by plotting the true positive rate against the false positive rate. The false positive rate is the probability of falsely rejecting the null hypothesis. For example, 70 of 1552 RMG-labeled and 8 of 3708 CRA-labeled alloys were categorized as BMG alloys by our VTS6-GFA model, and thus the false positive rate of predicting BMG using this model was 1.5%. The area under the ROC curve (AUC) can be applied to describe the performance of a classification model. AUC usually varies between 0.5 and 1, where 0.5 represents the uninformative classifier or so-called "random guess", a value > 0.95 represents an excellent classifier and a value = 1 is the perfect classifier. The AUC of classifying crystalline alloys and amorphous alloys classifications is 0.95, and the AUC of distinguishing BMG-labeled alloys from other alloys can reach 0.98. This excellent prediction accuracy indicates that our model can be used to discover new GFAs.

The GFA distributions of 6471 alloys with six SBS-chosen features are shown in Fig. 4c–e, and provide some information on the key features required for the formation of BMGs. Alloys should be composed of elements with significant differences in work function and heat of fusion; valence electrons might weaken the glass-forming ability; the boiling temperature of alloys cannot be high; and the presence of subfamily elements, such as La and Zr, might enhance the glass forming ability. The 764 incorrect predictions of our ML model are marked

with white crosses, and it was possible that the ML model incorrectly classified an alloy whose neighbors in the feature space had a different GFA.

3.2. The D_{max} model based on compositions

The D_{max} dataset was constructed from the GFA dataset by removing these BMGs which did not have the value of measured D_{max}. In this way, the D_{max} dataset has the same 35 first-generation features as those in the GFA dataset. Subsequently, 13 high-influence features were selected by VT and ReliefF to compare their performance. Finally, two six-feature subsets were selected by SBF and SFS with a 0.01 reduction of the correlation coefficient (r).

Fig. 5a shows that the ML model (CFS-D_{max}) on the CFS subset outperforms other feature subsets in the *k*-fold CV test. The ML model on the ReliefF subset ($r = 0.8542$) performs much better than the VT subset ($r = 0.8339$) in the *k*-fold CV test, i.e., features in the ReliefF subset are the second-generation features. It can be seen that the ML model based on the SBS-6 subset ($r = 0.8503$) has a similar r value to that of the SFS-6 subset ($r = 0.8511$). Fig. 5b indicates that the ML model applied to the SFS-6 subset ($S_{mix}/R, H_f d, H_{mix}, Wd, T_{b2}, K_1$) had a smaller RMSE than does SBS-6 ($AN_1, KD, T_m d, T_{b2}, ANd, T_b d$) in the *k*-fold CV test. The ML model applied to the SFS-5 subset ($S_{mix}/R, H_f d, H_{mix}, Wd, T_{b2}$) had an r value of 0.8419 and an RMSE of 1.2389 mm, and the
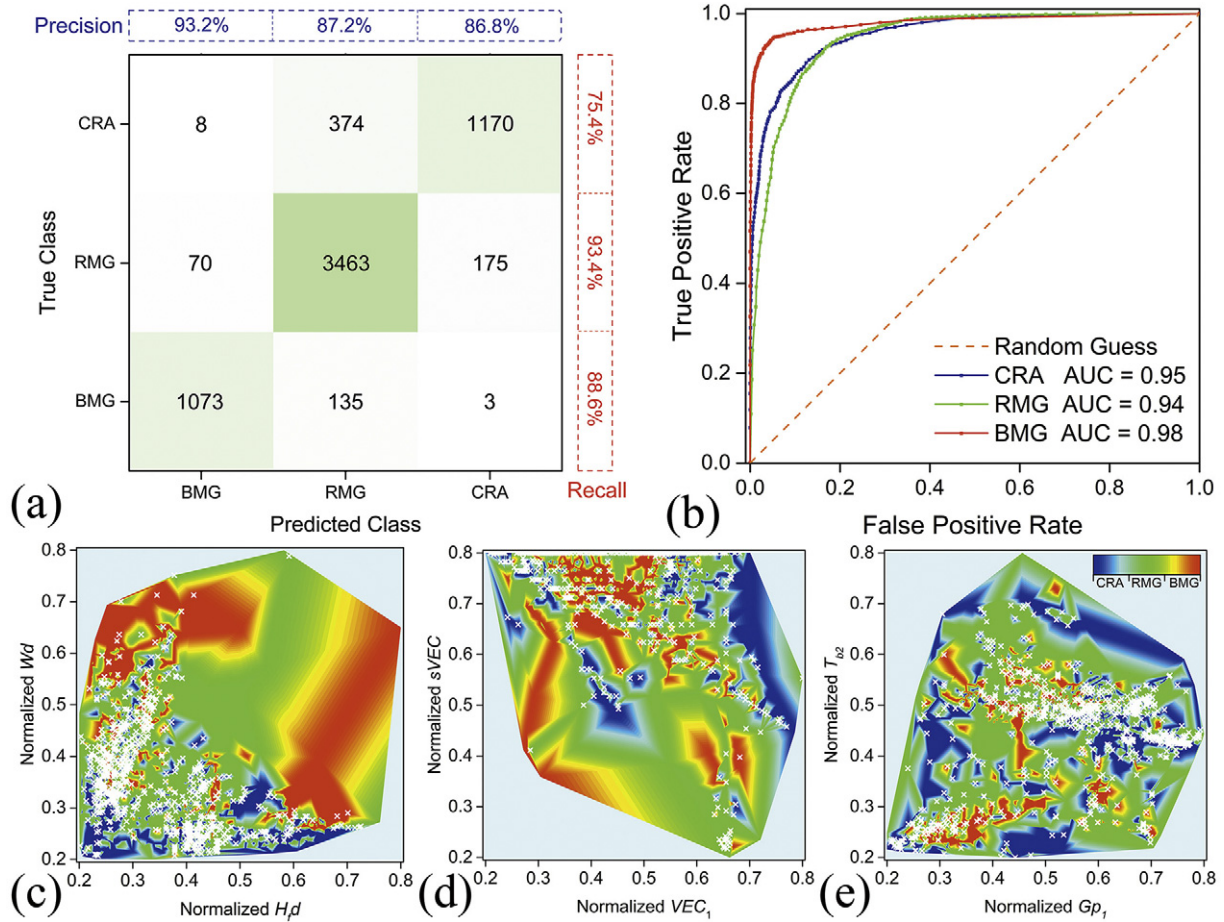
Fig. 4. The performance of the VTS6-GFA model shown as (a) the confusion matrix; (b) the receiver operating characteristic curve for distinguishing the CRA (red curve), RMG (green curve) and BMG (blue curve) alloys; the GFA distributions with (c) H_fd-Wd pair, (d) VEC_1-$sVEC$ pair and (e) Gp_1-T_{b2} pair, where the incorrect classifications of the VTS6-GFA model are marked with white crosses.

performance increased significantly ($r = 0.8511$, $RMSE = 1.2063$ mm) when adding feature K_1. Compared with the best-performing CFS-D_{max} model, 28 features were removed with only a 0.0089 reduction of r and 0.0272 mm increase of RMSE in the SFS-6 subset.

Fig. 5c shows a plot of the ML-predicted values against the measured values for D_{max} with the SFS-6 subset. Setting a ± 10 mm predicting

error yields nine outliers, six of them shown in Table 2 have an error bigger than ± 15 mm. The ML model applied to the SFS-6 subset (SFS6-D_{max}) significantly overestimated the D_{max} of $Zr_{41}Ti_{14}Cu_{12.5}Ni_8C_2Be_{22.5}$, which can be explained by the fact that it has a much lower D_{max} than a similar composition of $Zr_{41.2}Ti_{13.8}Cu_{12.5}Ni_{10}Be_{22.5}$. This also might be the reason for the underestimated D_{max} of $Zr_{41.2}Ti_{13.8}Cu_{12.5}Ni_{10}Be_{22.5}$.
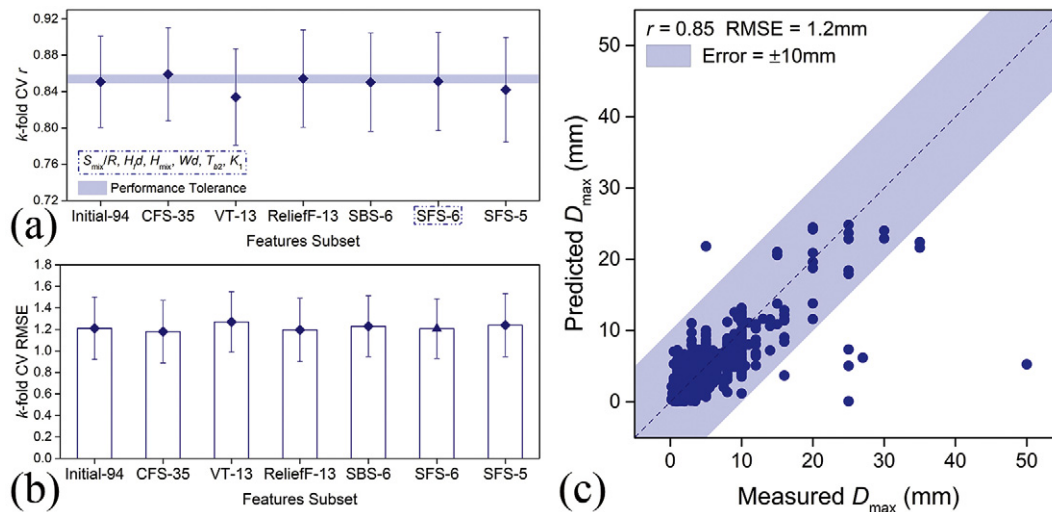

Fig. 5. The (a) r and (b) $RMSE$ of the random forest model applied to various feature subsets in k-fold CV. (c) ML-predicted values versus the measured values, with a ± 10 mm predicting error.

Table 2
Measured and predicted D_{max} of six outliers whose predicting error is bigger than ± 15 mm.

Alloy	Measured D_{max}	Predicted D_{max}
$Zr_{41}Ti_{14}Cu_{12.5}Ni_8C_2Be_{22.5}$	5 mm	21.8 mm
$Zr_{41.2}Ti_{13.8}Cu_{12.5}Ni_{10}Be_{22.5}$	50 mm	5.3 mm
$Y_{36}Sc_{20}Al_{24}Co_{20}$	25 mm	7.4 mm
$Y_{36}Sc_{20}Al_{24}Co_{10}Ni_{10}$	25 mm	5.1 mm
$Mg_{59.5}Cu_{22.9}Ag_{6.6}Gd_{11}$	27 mm	6.2 mm
$Pd_{40}Ni_{40}P_{20}$	25 mm	0.1 mm

There were four Al-Co-Sc-Y alloys and three $X_{36}Y_{20}Al_{24}Co_{20}$ (X = Sc, Gd, Y) alloys in our dataset, and most of these had measured D_{max} values <5 mm, except $Y_{36}Sc_{20}Al_{24}Co_{20}$. Thus, the D_{max} of $Y_{36}Sc_{20}Al_{24}Co_{20}$ and $Y_{36}Sc_{20}Al_{24}Co_{10}Ni_{10}$ were underestimated. The alloys $Mg_{65}Cu_{15}Ag_{10}Gd_{10}$ (measured D_{max} = 7.5 mm) and Ni-P-Pd RMG (measured D_{max} = 0.1 mm) perturbed the prediction of $Mg_{59.5}Cu_{22.9}Ag_{6.6}Gd_{11}$ and $Pd_{40}Ni_{40}P_{20}$, respectively. In summary, the discrepancies between predictions and observations might be caused by two reasons. The first is that the ML model is not able to predict the property that changes abruptly from its neighbors in the feature space. In this case, a more rigorous ML model should be developed to enhance the model capacity. The other reason is that some observations may not be reliable. More experiments should be conducted to ensure the reported experimental data. Reliable data are essential to ML, especially when the dataset is small. Overall, the SFS6-D_{max} model can predict the D_{max} of alloys well.

Symbolic regression (SR) was used to search for a parameter that can be generated using non-normalized features in the SFS-6 subset without the six outliers mentioned above, and with the integer constant, and the operators $\{+, -, \times, \div, \sqrt{\ }, \exp\}$. A series of parameters of D_{max} were generated with 1, 2, and 3 features, respectively. Next, three linear least-square (LLS) models were built with these parameters, revealing that the LLS model using γ_3 had the highest r value of 0.7125. Its performance in the k-fold CV test is shown in Fig. 6a.

Eqs. (21) and (22) indicate that a high S_{mix} (mixing entropy, $J \cdot mol^{-1} \cdot K^{-1}$) can promote GFA, which meets the confusion principle [55]. Eqs. (22) and (23) show that K_1 (the thermal conductivity, $W \cdot m^{-1} \cdot K^{-1}$) of a solid alloy will affect its GFA, and that high thermal conductivity might lead to a slow critical cooling rate, i.e. big casting diameter [56]. The influence of H_{mix} (mixing enthalpy, $kJ \cdot mol^{-1}$) can be seen in Eq. (23), where a weak mixing enthalpy fosters the formation of a solid-solution phase, and an ultra-negative mixing enthalpy leads to

the formation of a intermetallic phase [56]; both of these hinder glass formation. Thus, three prerequisites for forming BMGs are (1) a high mixing entropy, (2) a high average thermal conductivity, and (3) an appropriate negative mixing enthalpy, approximately equal to −28 kJ/mol $\left(\dfrac{\partial \gamma_3}{\partial H_{mix}} = 0 \right)$.

$$D_{max-1F} \propto \gamma_1 = \exp\left(\frac{-6}{S_{mix}/R} \right) \tag{21}$$

$$D_{max-2F} \propto \gamma_2 = K_1 \exp\left(\frac{-7}{(S_{mix}/R)^2} \right) \tag{22}$$

$$D_{max-3F} \propto \gamma_3 = (S_{mix}/R)^3 + \frac{K_1 S_{mix}/R - 78}{791 + 56H_{mix} + H_{mix}^2 + \exp(1917 - 1744 S_{mix}/R)} \tag{23}$$

3.3. D_{max} model based on CTTs

One RF model, one LLS model based on symbolic regression, and 20 LLS models based on previously proposed GFA criteria were built on the CTT dataset without six outliers described in Section 3.2. The performance of these models was compared by a k-fold CV text. It can be seen in Table 3 that the ML model (Fig. 6b) outperformed other formulas in the k-fold CV test, as it had a much higher r (0.7723) and smaller RMSE (2.8915 mm). The next best was the LLS model based on SR ($r = 0.6721$), and then the χ-criteria.

The PCC values of 94 feature candidates and three CTTs were calculated. The CTTs and six features, namely T_{m1}, H_{f1}, Gpd, Gp_1, X_{P1}, and X_Pd, were highly correlated with each other. Thus, the symbolic regression was conducted using these six non-normalized features, the integer constant, and the operators $\{+, -, \times, \div, \sqrt{\ }, \exp\}$. SR parameters were generated for T_g, T_x, and T_l, respectively, as given by Eqs. (24), (25), and (26):

$$T_g \propto \varphi_g = \frac{17}{37} T_{m1} - \left(\frac{H_{f1}^3}{148} + \frac{1354}{H_{f1}} \right) \tag{24}$$

$$T_x \propto \varphi_x = T_{m1} \tag{25}$$

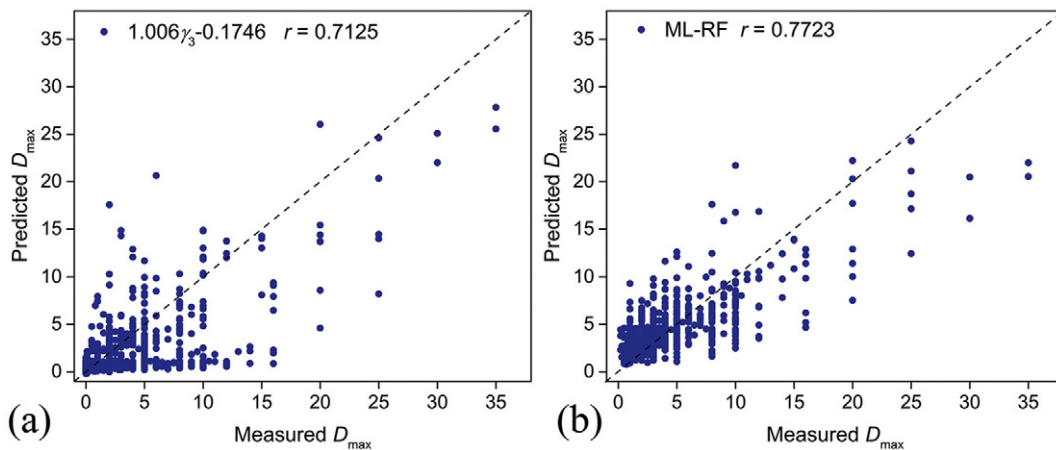$$T_l \propto \varphi_l = T_{m1} - 3R_{m1}T_{m1}. \tag{26}$$

Fig. 6. (a) The performance of LLSs based on the symbolic regression parameter γ_3 in the k-fold CV test. (b) The performance of the RF model on transition temperatures in the k-fold CV test.

Table 3
r values and *RMSE* values of the RF model and LLS model applied to the symbolic regression parameter and 20 GFA criteria.

GFA criteria	Formula	ref	R	RMSE
ΔT_x	$T_x - T_g$	[36]	0.4261	4.1121
T_{rg}	T_g/T_l	[37]	0.2047	4.4493
γ	$T_x/(T_g + T_l)$	[23]	0.4713	4.0089
ΔT_{rg}	$(T_x - T_g)/(T_l - T_g)$	[57]	0.5054	3.9221
α	T_x/T_l	[58]	0.4088	4.1482
β_M	$(T_x/T_g) + (T_g/T_l)$	[58]	0.4847	3.9757
δ	$T_x/(T_l - T_g)$	[59]	0.2951	4.3430
γ_m	$(2T_x - T_g)/T_l$	[60]	0.4934	3.9535
φ	$T_{rg}(\Delta T_x/T_g)^{0.143}$	[61]	0.4685	4.0157
ξ	$(T_g/T_l) + (\Delta T_x/T_x)$	[62]	0.4649	4.0243
β_Y	$(T_x T_g)/(T_l - T_x)^2$	[63]	0.3957	4.1745
$1/\omega_L$	$\omega_L = (T_g/T_x) - [2T_g/(T_g + T_l)]$	[64]	0.5362	3.8369
ω_J	$[T_l(T_l + T_x)]/[T_x(T_l - T_x)]$	[65]	0.4307	4.1024
θ	$[(T_x + T_g)/T_l] \cdot [(T_x - T_g)/T_l]^{0.0728}$	[66]	0.4438	4.0731
ω_A	$[T_g/(2T_x - T_g)] - (T_g/T_l)$	[67]	0.4972	3.9438
γ_c	$(3T_x - 2T_g)/T_l$	[68]	0.5136	3.9001
β'	$(T_g/T_x) - (T_g/1.3T_l)$	[69]	0.4890	3.9649
ω_B	$(2T_x - T_g)/(T_l + T_x)$	[70]	0.5036	3.9270
G_p	$[T_g(T_x - T_g)]/[(T_l - T_x)^2]$	[21]	0.5520	3.7901
χ	$[(T_x - T_g)/(T_l - T_x)] \cdot [T_x/(T_l - T_x)]^{1.47}$	[71]	0.5527	3.7883
RF	$D_{max} = f(T_g, T_x, T_l)$	This work	0.7723	2.8915
SR	$\dfrac{T_g^2}{T_l^3} + \dfrac{1940}{136263T_l - 1426T_l(T_x - T_g)} + \dfrac{T_g^2}{39T_l(14T_l - (T_x - T_g)^2)}$	This work	0.6721	3.3655

The SR results showed that T_g, T_x, and T_l (critical transition temperature, K) are largely and directly influenced by T_{m1} (average melting temperature, K), which is shown by the fact that $r > 0.93$ in Fig. 7a. Eq. (24) indicates that the glass transition temperature will increase then decrease as H_{f1} (average heat of fusion, kJ · mol^{-1}) increases. The liquidus temperature will increase as R_{m1} (average atomic radius, nm) decreases, and the small atomic radius might enhance the resistance of the alloy to phase transition.

3.4. EM model

In our previous work on the prediction of the mechanical properties of metal-metal amorphous alloys [72], four features (X_{p1}, V_{mm}, $R_m d$, and S_{mix}/R) were found to be crucial. Extending the results to the dataset built in this work, ML models have been constructed to predict the EM of metallic-metallic and metalloid-metallic bulk metallic glasses. The global optimization method and the exhaustive feature selection method was utilized in this low-dimensional feature space. Fifteen ML models were built on all possible subsets of four influential features, and the performance of these ML models was compared (as shown in Fig. 8a and b) to find the best predictive model for the shear (G) and bulk (B) moduli, respectively. The r value of the ML model for predicting shear moduli reached a maximum of 0.9836 when the subset contained

$R_m d$ and X_{p1}, and the RMSE reached a minimum of 3.609 GPa. The r value for bulk moduli reached a maximum of 0.9843 when the subset contained all features, and this decreased slightly to 0.9840 when $R_m d$ was removed. Thus, the subset containing X_{p1}, V_{mm}, and S_{mix}/R, which had an *RMSE* of 9.531 GPa, was considered as the best subset for bulk moduli.

Fig. 8c and d show the excellent predictive power of this subset, in the plot of the ML-predicted values against the measured values for G and B, respectively, with the best selected subset having three features. There are four exceptions, shown as Table 4 and dots outside the blue region. The high measured shear modulus (>75 GPa) of $Fe_{49}Cr_{15}Mo_{14}C_{15}B_6Er_1$ and $Fe_{50}Mn_{10}Mo_{14}Cr_4C_{16}B_6$, whose X_{p1} are close to $Ni_{80}P_{20}$, led to the overestimation of $Ni_{80}P_{20}$. The V_{mm} value of $Fe_{71}Nb_6B_{23}$ (measured $B = 182.6$ GPa) is similar to that of $Fe_{80}P_{11}C_9$; therefore, the ML model overestimated the modulus of $Fe_{80}P_{11}C_9$. The similarity of V_{mm} and X_{p1} values between $Pt_{74.7}Cu_{1.5}Ag_{0.3}P_{18.0}B_{4.0}Si_{1.5}$ and $Au_{49.0}Ag_{5.5}Pd_{2.3}Cu_{26.9}Si_{16.3}$ led to the incorrect ML model-based prediction of their bulk moduli.

The SR parameters α and β were generated using four non-normalized features, the integer constant, and the operators $\{+, -, \times, \div, \sqrt{\ }, \exp\}$. The performances of LLS models built on two-features parameters in the k-fold CV test are shown in Fig. 9. The LLS models based on these SR parameters all performed well, with $r > 0.93$.
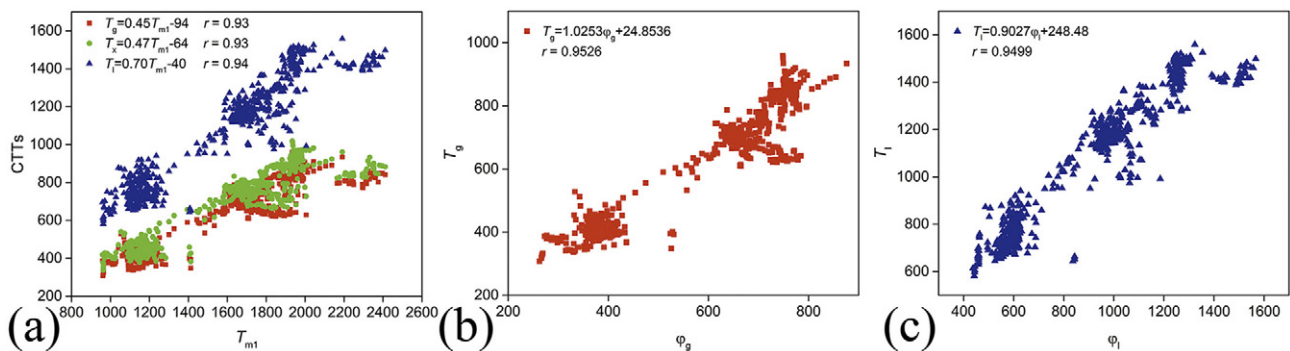

Fig. 7. (a) The linear relationship between the critical transformation temperature and average melting temperatures. The performances of linear least square models based on symbolic regression parameter (b) φ_g and (c) φ_l in a k-fold cross-validation test.
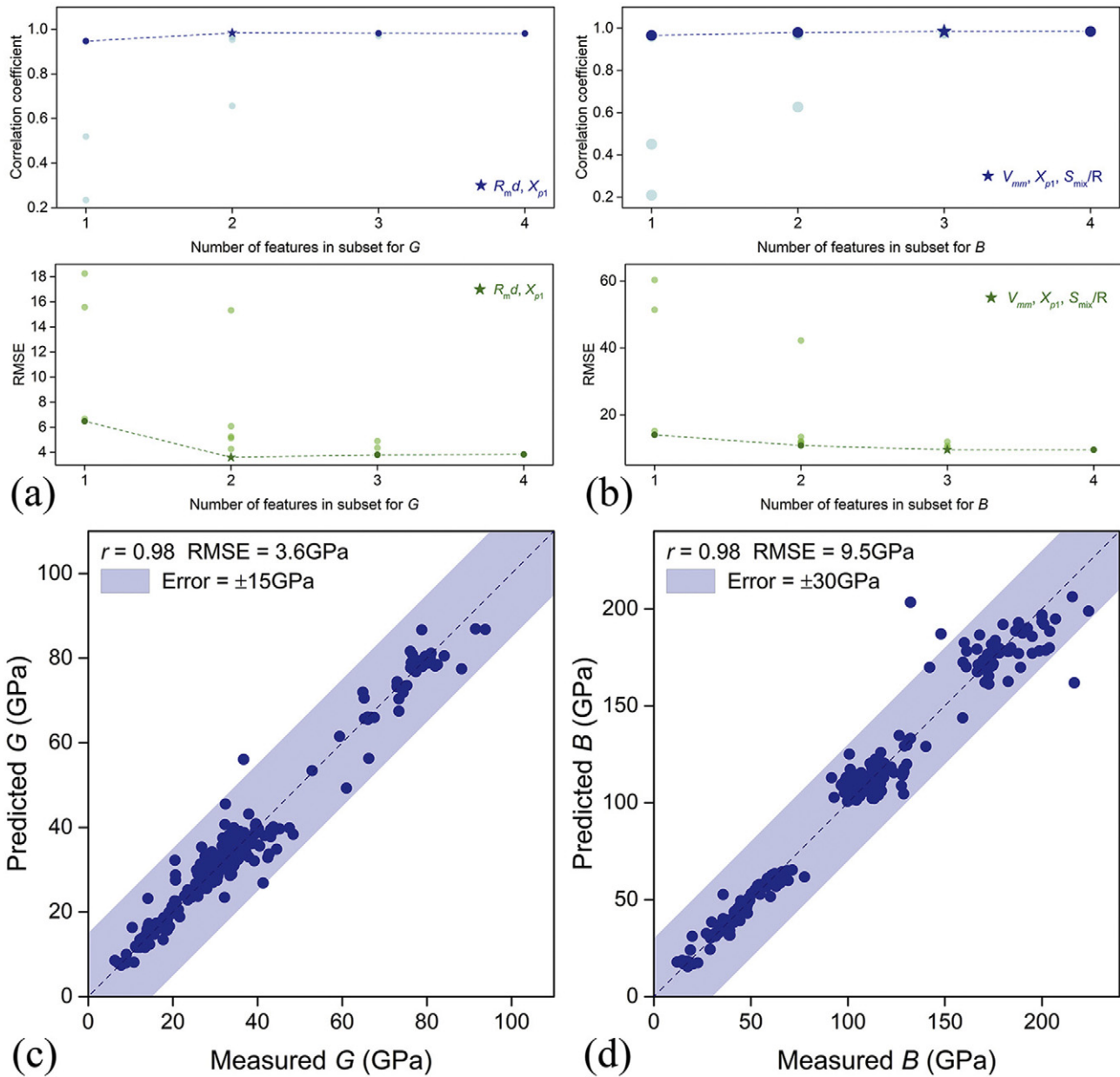
Fig. 8. The performance of RF models on all possible subsets of four influential features in predicting (a) shear moduli and (b) bulk moduli. The performance of the ML model on the best subset of three features in predicting (c) shear moduli with a ±15 GPa error and (d) bulk moduli with a ±30 GPa error.

The SR results are given by Eqs. (27)–(29), and show that a smaller V_{mm} (average atomic volume, Å³) results in a higher G (shear modulus, GPa) and B (bulk modulus, GPa). Eq. (28) supports Park's work, as it shows that high mixing entropy coupled with disordered amorphous structure manifests small shear transformation zone sizes, which could make the shear bands more difficult to form and propagate,

leading to higher shear moduli [73]. When considering Pauling electronegativity, higher electronegativity corresponds to stronger atomic bonding, and therefore higher bulk moduli.

$$G_{1F} \propto \alpha_1 = \frac{1}{V_{mm}} \tag{27}$$

$$G_{2F} \propto \alpha_2 = \frac{1}{V_{mm} - 2S_{mix}/R} \tag{28}$$

$$B_{1F} \propto \beta_1 = \frac{1}{4169 + 2V_{mm}^3} \tag{29}$$

$$B_{2F} \propto \beta_2 = \frac{1366 X_{P1}^2}{V_{mm} + 4X_{P1}^2} + \frac{456}{214 - V_{mm}^2} \tag{30}$$

Table 4
Measured and predicted elastic modulus of four exceptions.

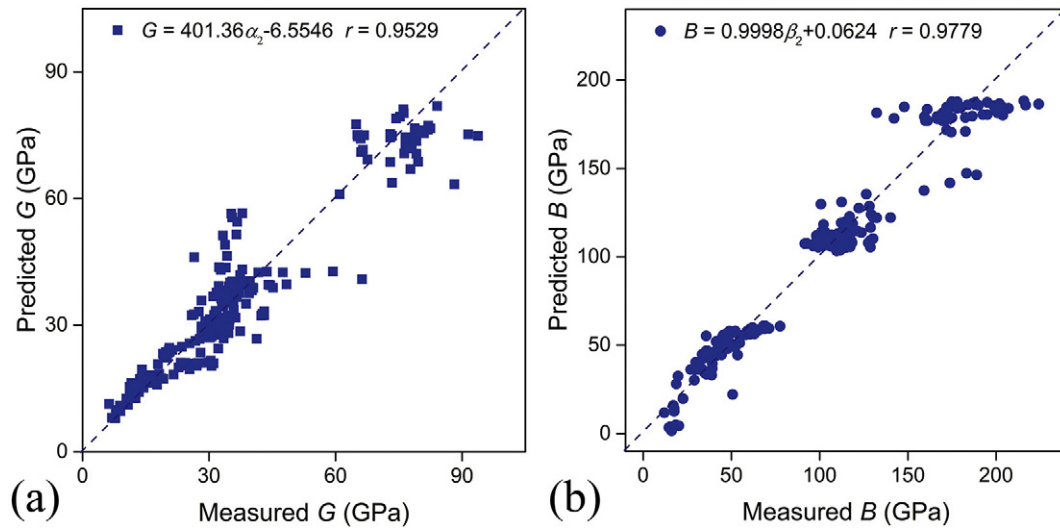| Alloy	Measured EM	Predicted EM
$Ni_{80}P_{20}$	$G = 36.7$ GPa	$G = 56.1$ GPa
$Fe_{80}P_{11}C_9$	$B = 148$ GPa	$B = 187$ GPa
$Pt_{74.7}Cu_{1.5}Ag_{0.3}P_{18.0}B_{4.0}Si_{1.5}$	$B = 216.7$ GPa	$B = 161.9$ GPa
$Au_{49.0}Ag_{5.5}Pd_{2.3}Cu_{26.9}Si_{16.3}$	$B = 132.3$ GPa	$B = 203.4$ GPa

Fig. 9. The performance of the LLS based on SR parameters in predicting (a) shear moduli and (b) bulk moduli.

3.5. Experimental validation and iterations

We address a design problem as finding new kinds of BMG alloys. In this section, we will show a ML solution for this issue.

The ability to form a bulk metallic glass was not measured during melt spinning, i.e., the bulk-forming ability of an RMG alloy is unknown. This limits the ability of the ML model to classify RMG alloys, especially distinguish RMG from BMG alloys. Thus, we can find new BMG alloys from RMG alloys (shown as Table S2) which are categorized as BMG alloys by the VTS6-GFA model. Thirteen RMGs with a high probability (>60%) of belonging to BMG were chosen and their glass-forming ability were rechecked, five of them, $La_{55}Al_{20}Cu_{25}$ [74], $Zr_{60}Al_{15}Cu_{25}$ [75], $Pd_{56}Ni_{24}P_{20}$ [76], $Mg_{65}Cu_{25}Ce_{10}$ [77], and $La_{50}Al_{25}Cu_{25}$ [78] are found to form bulk samples. The classification performance of the VTS6-GFA model improved as shown in Fig. 10. Those validations and iterations confirm the correctness, generalization and predictive ability of our ML model.

4. Conclusion

In this study, we have presented a general ML framework for the prediction, design, and understanding of metallic glasses. These models were constructed based on datasets built from metallic glass experiments comprising over 6000 samples. We used these datasets to train and cross-validate ML models with an RF algorithm to predict the GFA, D_{max}, shear moduli, and bulk moduli. A three-step feature selection method was proposed for ML, and it performed well with the GFA and D_{max} models.

Based on the ML-based GFA model, BMGs should be composed of elements with significant differences in work function and heat of fusion; valence electrons might weaken the glass-forming ability; the boiling temperature of alloys cannot be high; and the presence of subfamily elements might enhance the glass forming ability.

In addition, mathematical expressions were generated from SR and LLSs for regression problems. Three properties that favor the formation of BMGs with large casting diameters were proposed, as follows: (1) high mixing entropy, (2) high average thermal conductivity, and (3) appropriate negative mixing enthalpy, of approximately −28 kJ/ mol. The CTTs of metallic glasses were thus determined to be largely and directly influenced by the average melting temperatures of the alloys of which they are composed. The shear and bulk moduli of BMGs are negatively correlated with the average atomic volume of the constituent alloys, the mixing entropy enhance the shear moduli and the average Pauling electronegativity influences the bulk moduli of BMGs.

This ML framework can guide the discovery and understanding of new BMGs with desired properties.

CRediT authorship contribution statement

Jie Xiong: Conceptualization, Investigation, Methodology, Data curation, Writing - original draft. **San-Qiang Shi:** Writing - review & editing, Funding acquisition. **Tong-Yi Zhang:** Writing - review & editing, Funding acquisition.
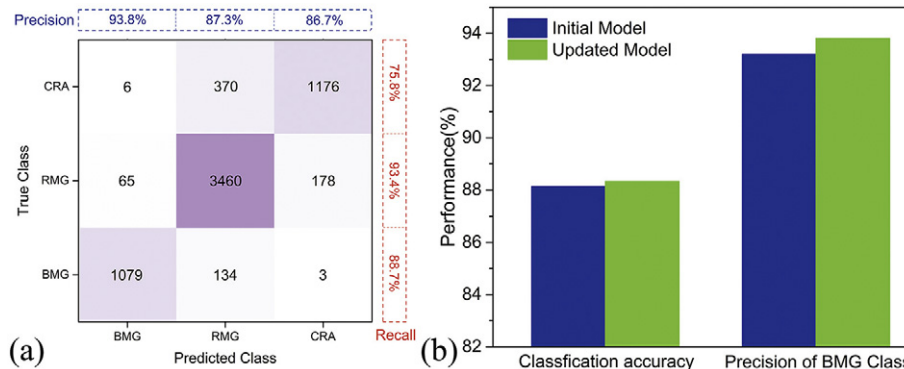

Fig. 10. (a) The performance of the updated VTS6-GFA model shown as the confusion matrix; (b) comparison of the classification accuracy and precision of BMG on initial model and updated model with feedback.

Declaration of competing interest

Acknowledgments

Appendix A. Supplementary data

Supplementary data to this article can be found online at https://doi.org/10.1016/j.matdes.2019.108378.

References

[1] L. Zhang, H. Huang, Micro machining of bulk metallic glasses: a review, Int. J. Adv. Manuf. Technol. (2019) https://doi.org/10.1007/s00170-018-2726-y.

[2] M. Jafary-Zadeh, G.P. Kumar, P.S. Branicio, M. Seifi, J.J. Lewandowski, F. Cui, A critical review on metallic glasses as structural materials for cardiovascular stent applications, J. Funct. Biomater. (2018) https://doi.org/10.3390/jfb9010019.

[3] M.M. Khan, A. Nemati, Z.U. Rahman, U.H. Shah, H. Asgar, W. Haider, Recent advancements in bulk metallic glasses and their applications: a review, Crit. Rev. Solid State Mater. Sci. (2018) https://doi.org/10.1080/10408436.2017.1358149.

[4] B. Nair, B.G. Priyadarshini, Process, structure, property and applications of metallic glasses, AIMS Mater. Sci. (2016) https://doi.org/10.3934/matersci.2016.3.1022.

[5] J.D. Schuler, T.J. Rupert, Materials selection rules for amorphous complexion formation in binary metallic alloys, Acta Mater. 140 (2017) 196–205, https://doi.org/10.1016/j.actamat.2017.08.042.

[6] M.W. Chen, A brief overview of bulk metallic glasses, NPG Asia Mater 3 (2011) 82–90, https://doi.org/10.1038/asiamat.2011.30.

[7] Y. Li, Y. Liu, Z. Liu, S. Sohn, F.J. Walker, J. Schroers, S. Ding, Combinatorial development of bulk metallic glasses, Nat. Mater. 13 (2014) 494–500, https://doi.org/10.1038/nmat3939.

[8] D. Kim, B.J. Lee, N.J. Kim, Prediction of composition dependency of glass forming ability of Mg-Cu-Y alloys by thermodynamic approach, Scr. Mater. 52 (2005) 969–972, https://doi.org/10.1016/j.scriptamat.2005.01.038.

[9] S.W. Kao, C.C. Hwang, T.S. Chin, Simulation of reduced glass transition temperature of Cu-Zr alloys by molecular dynamics, J. Appl. Phys. 105 (2009) https://doi.org/10.1063/1.3086623.

[10] D.V. Louzguine-Luzgin, R. Belosludov, M. Saito, Y. Kawazoe, A. Inoue, Glass-transition behavior of Ni: calculation, prediction, and experiment, J. Appl. Phys. 104 (2008) https://doi.org/10.1063/1.3042240.

[11] J.J. Pang, M.J. Tan, K.M. Liew, On valence electron density, energy dissipation and plasticity of bulk metallic glasses, J. Alloys Compd. 577 (2013) S56–S65, https://doi.org/10.1016/j.jallcom.2012.03.036.

[12] A. Takeuchi, A. Inoue, Classification of bulk metallic glasses by atomic size difference, heat of mixing and period of constituent elements and its application to characterization of the main alloying element, Mater. Trans. 46 (2005) 2817–2829, https://doi.org/10.2320/matertrans.46.2817.

[13] Y. Sato, C. Nakai, M. Wakeda, S. Ogata, Predictive modeling of time-temperature-transformation diagram of metallic glasses based on atomistically-informed classical nucleation theory, Sci. Rep. 7 (2017) https://doi.org/10.1038/s41598-017-06482-8.

[14] D.Z. Xue, P.V. Balachandran, J. Hogden, J. Theiler, D.Q. Xue, T. Lookman, Accelerated search for materials with targeted properties by adaptive design, Nat. Commun. 7 (2016) https://doi.org/10.1038/ncomms11241.

[15] D.Z. Xue, D.Q. Xue, R.H. Yuan, Y.M. Zhou, P.V. Balachandran, X.D. Ding, J. Sun, T. Lookman, An informatics approach to transformation temperatures of NiTi-based shape memory alloys, Acta Mater. 125 (2017) 532–541, https://doi.org/10.1016/j.actamat.2016.12.009.

[16] C. Wen, Y. Zhang, C.X. Wang, D.Z. Xue, Y. Bai, S. Antonov, L.H. Dai, T. Lookman, Y.J. Su, Machine learning assisted design of high entropy alloys with desired property, Acta Mater. 170 (2019) 109–117, https://doi.org/10.1016/j.actamat.2019.03.010.

[17] S. Feng, H.Y. Zhou, H.B. Dong, Using deep neural network with small dataset to predict material defects, Mater. Des. 162 (2019) 300–310, https://doi.org/10.1016/j.matdes.2018.11.060.

[18] Y.T. Sun, H.Y. Bai, M.Z. Li, W.H. Wang, Machine learning approach for prediction and understanding of glass-forming ability, J. Phys. Chem. Lett. 8 (2017) 3434–3439, https://doi.org/10.1021/acs.jpclett.7b01046.

[19] C. Wolverton, G.R. Jelbert, S.C. O'Keeffe, J. Stevick, M. Aykol, L. Ward, A machine learning approach for engineering bulk metallic glass alloys, Acta Mater. 159 (2018) 102–111, https://doi.org/10.1016/j.actamat.2018.08.002.

[20] F. Ren, L. Ward, T. Williams, K.J. Laws, C. Wolverton, J. Hattrick-Simpers, A. Mehta, Accelerated discovery of metallic glasses through iteration of machine learning and high-throughput experiments, Sci. Adv. 4 (2018) https://doi.org/10.1126/sciadv.aaq1566.

[21] M.K. Tripathi, S. Ganguly, P. Dey, P.P. Chattopadhyay, Evolution of glass forming ability indicator by genetic programming, Comput. Mater. Sci. 118 (2016) 56–65, https://doi.org/10.1016/j.commatsci.2016.02.037.

[22] M.K. Tripathi, P.P. Chattopadhyay, S. Ganguly, Multivariate analysis and classification of bulk metallic glasses using principal component analysis, Comput. Mater. Sci. 107 (2015) 79–87, https://doi.org/10.1016/j.commatsci.2015.05.010.

[23] Z.P. Lu, C.T. Liu, A new glass-forming ability criterion for bulk metallic glasses, Acta Mater. 50 (2002) 3501–3512, https://doi.org/10.1016/S1359-6454(02)00166-0.

[24] Z.L. Long, H.Q. Wei, Y.H. Ding, P. Zhang, G.Q. Xie, A. Inoue, A new criterion for predicting the glass-forming ability of bulk metallic glasses, J. Alloys Compd. 475 (2009) 207–219, https://doi.org/10.1016/j.jallcom.2008.07.087.

[25] J.W. Li, A.N. He, B.L. Shen, Effect of Tb addition on the thermal stability, glass-forming ability and magnetic properties of Fe-B-Si-Nb bulk metallic glass, J. Alloys Compd. 586 (2014) S46–S49, https://doi.org/10.1016/j.jallcom.2012.09.087.

[26] S. Tao, T.Y. Ma, H. Jian, Z. Ahmad, H. Tong, M. Yan, Glass forming ability, magnetic and mechanical properties of $(Fe_{72}Mo_4B_{24})_{(100-x)}Dy_x$ (x=4-7) bulk metallic glasses, Mater. Sci. Eng. A 528 (2010) 161–164, https://doi.org/10.1016/j.msea.2010.08.092.

[27] K.F. Xie, K.F. Yao, T.Y. Huang, Preparation of $(Ti_{0.45}Cu_{0.378}Zr_{0.10}Ni_{0.072})_{(100-x)}Sn_x$ bulk metallic glasses, J. Alloys Compd. 504 (2010) S22–S26, https://doi.org/10.1016/j.jallcom.2010.02.199.

[28] N.B. Hua, R. Li, H. Wang, J.F. Wang, Y. Li, T. Zhang, Formation and mechanical properties of Ni-free Zr-based bulk metallic glasses, J. Alloys Compd. 509 (2011) S175–S178, https://doi.org/10.1016/j.jallcom.2011.01.078.

[29] C. Suryanarayana, A. Inoue, Iron-based bulk metallic glasses, Int. Mater. Rev. 58 (2012) 131–166, https://doi.org/10.1179/1743280412y.0000000007.

[30] Q.S. Zhang, W. Zhang, D.V. Louzguine-Luzgin, A. Inoue, Effect of substituting elements on glass-forming ability of the new $Zr_{48}Cu_{36}Al_8Ag_8$ bulk metallic glass-forming alloy, J. Alloys Compd. 504 (2010) S18–S21, https://doi.org/10.1016/j.jallcom.2010.02.052.

[31] W. Jiao, D.Q. Zhao, D.W. Ding, H. Bai, W.H. Wang, Effect of free electron concentration on glass-forming ability of Ca-Mg-Cu system, J. Non-Cryst. Solids 358 (2012) 711–714, https://doi.org/10.1016/j.jnoncrysol.2011.10.033.

[32] F. Yuan, J. Du, B.L. Shen, Controllable spin-glass behavior and large magnetocaloric effect in Gd-Ni-Al bulk metallic glasses, Appl. Phys. Lett. 101 (2012) https://doi.org/10.1063/1.4738778.

[33] M.X. Pan, A.L. Greer, W.H. Wang, B. Zhang, D.Q. Zhao, Amorphous metallic plastic, Phys. Rev. Lett. 94 (2005) 1–4, https://doi.org/10.1103/physrevlett.94.205502.

[34] W.H. Wang, The elastic properties, elastic models and elastic perspectives of metallic glasses, Prog. Mater. Sci. 57 (2012) 487–656, https://doi.org/10.1016/j.pmatsci.2011.07.001.

[35] Y. Kawazoe, T. Masumoto, K. Suzuki, A. Inoue, A.-P. Tsai, J.-Z. Yu, T. Aihara Jr., T. Nakanomyo, Nonequilibrium Phase Diagrams of Ternary Amorphous Alloys, Springer-Verlag, Berlin/Heidelberg, 1997 https://doi.org/10.1007/b58222.

[36] A. Inoue, Stabilization of metallic supercooled liquid, Acta Mater. 48 (2000) 279–306, https://doi.org/10.1016/S1359-6454(99)00300-6.

[37] Z.P. Lu, Y. Li, S.C. Ng, Reduced glass transition temperature and glass forming ability of bulk glass forming alloys, J. Non-Cryst. Solids (2000) https://doi.org/10.1016/S0022-3093(00)00064-8.

[38] W.H. Wang, Correlations between elastic moduli and properties in bulk metallic glasses, J. Appl. Phys. 99 (2006) https://doi.org/10.1063/1.2193060.

[39] X.Q. Chen, H. Niu, D. Li, Y. Li, Modeling hardness of polycrystalline materials and bulk metallic glasses, Intermetallics 19 (2011) 1275–1281, https://doi.org/10.1016/j.intermet.2011.03.026.

[40] C. Carruthers, H. Teitelbaum, The linear mixture rule in chemical-kinetics. II. Thermal-dissociation of diatomic-molecules, Chem. Phys. 127 (1988) 351–362, https://doi.org/10.1016/0301-0104(88)87133-7.

[41] R.H. McKee, A.M. Medeiros, W.C. Daughtrey, A proposed methodology for setting occupational exposure limits for hydrocarbon solvents, J. Occup. Environ. Hyg. 2 (2005) 524–542, https://doi.org/10.1080/15459620500299754.

[42] S.S. Fang, X. Xiao, X. Lei, W.H. Li, Y.D. Dong, Relationship between the widths of supercooled liquid regions and bond parameters of Mg-based bulk metallic glasses, J. Non-Cryst. Solids 321 (2003) 120–125, https://doi.org/10.1016/S0022-3093(03)00155-8.

[43] P.K. Ray, M. Akinc, M.J. Kramer, Applications of an extended Miedema's model for ternary alloys, J. Alloys Compd. 489 (2010) 357–361, https://doi.org/10.1016/j.jallcom.2009.07.062.

[44] R. Guthrie, T. Iida, The Thermophysical Properties of Metallic Liquids, Oxford University Press (2015).

[45] B.R. Rao, M. Srinivas, A.K. Shah, A.S. Gandhi, B.S. Murty, A new thermodynamic parameter to predict glass forming ability in iron based multi-component systems containing zirconium, Intermetallics 35 (2013) 73–81, https://doi.org/10.1016/j.intermet.2012.11.020.

[46] L. Ward, A. Agrawal, A. Choudhary, C. Wolverton, A general-purpose machine learning framework for predicting properties of inorganic materials, NPJ Comput. Mater. 2 (2016) 1–7, https://doi.org/10.1038/npjcompumats.2016.28.

[47] J.Q. Wang, W.H. Wang, H.B. Yu, H.Y. Bai, Correlations between elastic moduli and molar volume in metallic glasses, Appl. Phys. Lett. 94 (2009) https://doi.org/10.1063/1.3106110.

[48] L. Friedman, O.V. Komogortsev, Assessment of the effectiveness of seven biometric feature normalization techniques, IEEE T. Inf. Foren. Sec. 14 (2019) 2528–2536, https://doi.org/10.1109/Tifs.2019.2904844.

[49] Z. Tang, P.A. Fishwick, Feedforward neural nets as models for time series forecasting, ORSA J. Comput. (1993) https://doi.org/10.1287/ijoc.5.4.374.

[50] R.J. Palma-Mendoza, D. Rodriguez, L. de-Marcos, Distributed ReliefF-based feature selection in Spark, Knowl. Inf. Syst. 57 (2018) 1–20, https://doi.org/10.1007/s10115-017-1145-y.

[51] J.D. Li, K.W. Cheng, S.H. Wang, F. Morstatter, R.P. Trevino, J.L. Tang, H. Liu, Feature selection: a data perspective, ACM Comput. Surv. 50 (2018) https://doi.org/10.1145/3136625.

[52] R.R. Bouckaert, E. Frank, M. Hall, R. Kirkby, P. Reutemann, A. Seewald, D. Scuse, WEKA Manual for Version 3-8-3, University of Waikato, 2018.

[53] S. Sun, R.H. Ouyang, B.C. Zhang, T.Y. Zhang, Data-driven discovery of formulas by symbolic regression, MRS Bull. 44 (2019) 559–564, https://doi.org/10.1557/mrs.2019.156.

[55] C. Chattopadhyay, B.S. Murty, Kinetic modification of the "confusion principle" for metallic glass formation, Scr. Mater. 116 (2016) 7–10, https://doi.org/10.1016/j.scriptamat.2016.01.022.

[56] D.B. Miracle, O.N. Senkov, A critical review of high entropy alloys and related concepts, Acta Mater. 122 (2017) 448–511, https://doi.org/10.1016/j.actamat.2016.08.081.

[57] X.S. Xiao, F. Shoushi, G.M. Wang, H. Qin, Y. Dong, Influence of beryllium on thermal stability and glass-forming ability of Zr-Al-Ni-Cu bulk amorphous alloys, J. Alloys Compd. 376 (2004) 145–148, https://doi.org/10.1016/j.jallcom.2004.01.014.

[58] K. Mondal, B.S. Murty, On the parameters to assess the glass forming ability of liquids, J. Non-Cryst. Solids 351 (2005) 1366–1371, https://doi.org/10.1016/j.jnoncrysol.2005.03.006.

[59] Q. Chen, J. Shen, D. Zhang, H. Fan, J. Sun, D.G. McCartney, A new criterion for evaluating the glass-forming ability of bulk metallic glasses, Mater. Sci. Eng. A 433 (2006) 155–160, https://doi.org/10.1016/j.msea.2006.06.053.

[60] X.H. Du, J.C. Huang, C.T. Liu, Z.P. Lu, New criterion of glass forming ability for bulk metallic glasses, J. Appl. Phys. 101 (2007) 2005–2008, https://doi.org/10.1063/1.2718286.

[61] G.J. Fan, H. Choo, P.K. Liaw, A new criterion for the glass-forming ability of liquids, J. Non-Cryst. Solids (2007) https://doi.org/10.1016/j.jnoncrysol.2006.08.049.

[62] X.H. Du, J.C. Huang, New criterion in predicting glass forming ability of various glass-forming systems, Chinese Phys. B. 17 (2008) 249–254, https://doi.org/10.1088/1674-1056/17/1/043.

[63] Z.Z. Yuan, S.L. Bao, Y. Lu, D.P. Zhang, L. Yao, A new criterion for evaluating the glass-forming ability of bulk glass forming alloys, J. Alloys Compd. 459 (2008) 251–260, https://doi.org/10.1016/j.jallcom.2007.05.037.

[64] Z.L. Long, G.Q. Xie, H.Q. Wei, X.P. Su, J. Peng, P. Zhang, A. Inoue, On the new criterion to assess the glass-forming ability of metallic alloys, Mater. Sci. Eng. A 509 (2009) 23–30, https://doi.org/10.1016/j.msea.2009.01.063.

[65] X.L. Ji, Y. Pan, A thermodynamic approach to assess glass-forming ability of bulk metallic glasses, T. Nonferr. Metal SOC. 19 (2009) 1271–1279, https://doi.org/10.1016/S1003-6326(08)60438-0.

[66] G.H. Zhang, K.C. Chou, A criterion for evaluating glass-forming ability of alloys, J. Appl. Phys. 106 (2009) https://doi.org/10.1063/1.3255952.

[67] H.Q. Wei, Z.L. Long, Z.C. Zhang, X.A. Li, J. Peng, P. Zhang, Correlations between viscosity and glass-forming ability in bulk amorphous alloys, Acta Phys. Sin. 58 (2009) 2556–2564, https://doi.org/10.7498/aps.58.2556.

[68] S. Guo, C.T. Liu, New glass forming ability criterion derived from cooling consideration, Intermetallics 18 (2010) 2065–2068, https://doi.org/10.1016/j.intermet.2010.06.012.

[69] B.S. Dong, S.X. Zhou, D.R. Li, C.W. Lu, F. Guo, X.J. Ni, Z.C. Lu, A new criterion for predicting glass forming ability of bulk metallic glasses and some critical discussions, Prog. Nat. Sci. Mater. Int. 21 (2011) 164–172, https://doi.org/10.1016/S1002-0071(12)60051-3.

[70] P. Blyskun, P. Maj, M. Kowalczyk, J. Latuch, T. Kulik, Relation of various GFA indicators to the critical diameter of Zr-based BMGs, J. Alloys Compd. 625 (2015) 13–17, https://doi.org/10.1016/j.jallcom.2014.11.112.

[71] Y. Zhang, M. Zhao, Z. Chen, W. Liu, Z. Long, M. Zhong, G. Liao, A new correlation between the characteristics temperature and glass-forming ability for bulk metallic glasses, J. Therm. Anal. Calorim. 132 (2018) 1645–1660, https://doi.org/10.1007/s10973-018-7050-0.

[72] J. Xiong, T.Y. Zhang, S.Q. Shi, Machine learning prediction of elastic properties and glass-forming ability of bulk metallic glasses, MRS Commun 9 (2019) 576–585, https://doi.org/10.1557/mrc.2019.44.

[73] E.S. Park, Understanding of the shear bands in amorphous metals, Appl. Microsc. (2015) https://doi.org/10.9729/am.2015.45.2.63.

[74] A.S. Argon, The Physics of Deformation and Fracture of Polymers, Cambridge University Press, 2010 https://doi.org/10.1017/CBO9781139033046.

[75] P.J. Tao, Q. Tu, W.W. Zhang, D.Y. Li, Investigation for biocompatibility of zirconium-based bulk metallic glasses with and without Ni element addition, Basic Clin. Pharmacol. 119 (2016) 10.

[76] R. Xu, W. Pang, Q. Huo, Modern Inorganic Synthetic Chemistry, Elsevier, 2011 https://doi.org/10.1016/C2009-0-30549-8.

[77] X.K. Xi, D.Q. Zhao, M.X. Pan, W.H. Wang, On the criteria of bulk metallic glass formation in MgCu-based alloys, Intermetallics 13 (2005) 638–641, https://doi.org/10.1016/j.intermet.2004.10.003.

[78] V. Kokotin, Polyhedra-Based Analysis of Computer Simulated, Technical University Dresden, 2010.
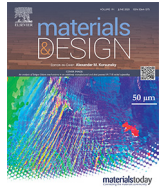
Update

Materials & Design

Corrigendum

Corrigendum to "A machine-learning approach to predicting and understanding the properties of amorphous metallic alloys" [Mat. Des., Volume 187 (2020), 108378]

Jie Xiong [b], San-Qiang Shi [b,*], Tong-Yi Zhang [a,*]

[a] Material Genome Institute, Shanghai University, Shanghai, China
[b] Department of Mechanical Engineering, The Hong Kong Polytechnic University, Hong Kong, China

The authors regret to inform that there is typo in the paper, the correct form of the Eq. (7) should be:

$$S_{mis}/k_B \cong (100R_m d)^2/21.92^2$$

Author would like to apologize for the inconvenience caused.